Numerical models of broad-bandwidth nanosecond optical parametric oscillators

A. V. Smith and Russell J. Gehr

Department 1128, Lasers, Optics and Remote Sensing, Sandia National Laboratories, Albuquerque, New Mexico 87185-1423

Mark S. Bowers

Aculight Corporation, 11805 North Creek Parkway South, Suite 113, Bothell, Washington 98011

We present three new methods for modeling broad-bandwidth, nanosecond optical parametric oscillators in the plane-wave approximation. Each accounts for the group-velocity differences that determine the operating linewidth of unseeded optical parametric oscillators, and each allows the signal and the idler waves to develop from quantum noise. The first two methods are based on split-step integration methods in which nonlinear mixing and propagation are calculated separately on alternate steps. One method relies on Fourier transforming the fields between t and ω to handle propagation, with mixing integrated over a Δz step; the other transforms between z and k_z in the propagation step, with mixing integrated over Δt. The third method is based on expansion of the three optical fields in terms of their respective longitudinal empty cavity modes, taking into account the cavity boundary conditions. Equations describing the time development of the mode amplitudes are solved to yield the time dependence of the three output fields. These models exclude diffraction and group-velocity dispersion but can be readily extended to include them. © 1999 Optical Society of America [S0740-3224(99)02103-7]

OCIS codes: 190.2620, 190.4410, 190.4970, 230.4320, 140.3430.

1. INTRODUCTION

In recent years the discovery of new nonlinear optical materials, improvements in the performance of solid-state pump lasers, and progress in high-damage-threshold optics has stimulated renewed interest in optical parametric oscillators (OPO's). Despite recent progress, these devices have yet to reach their full potential as sources with broad tunability, narrow linewidth, and good beam quality. One reason is that their behavior is more complex than is often appreciated. This complexity makes computer simulations essential in interpreting laboratory observations and in optimizing OPO designs. We reported earlier on a numerical model[1] of nanosecond, pulsed OPO's that included diffraction, birefringent walk-off, and pump depletion. Its predictions agreed well with detailed measurements of spatial beam profiles and beam quality, spatially resolved temporal pulse shapes, and frequency spectra for a single-frequency, injection-seeded KTP ring OPO. The primary limitation of that model was its assumption of narrow-bandwidth operation, which is appropriate for injection-seeded, single-longitudinal-mode devices pumped by single-longitudinal-mode pulses, but not for broad-bandwidth operation or for multi-longitudinal-mode pumps. To address this shortcoming, we present here three new methods for modeling multimode, or broad-bandwidth, OPO's pumped by single-mode or multimode lasers, in the plane-wave limit. Each method can be extended to include diffraction and birefringent walk-off, but that work is deferred, in part

because of the computing power required for such a complete model.

These models of broad-bandwidth OPO's should prove useful in understanding the spectral properties of unseeded, or free-running, pulsed OPO's that start from quantum noise, and also in understanding the conditions necessary for injection seeding them. For example, we noted in an earlier paper[2] that a free-running, pulsed OPO generated broadband light with nearly pure phase modulation. The models presented here can test the generality of this observation. They can also be useful in predicting line widths and efficiencies of free running OPO's, and with realistic quantum-noise models, they can predict the pulse-to-pulse fluctuations in output spectra and conversion efficiency. They should also answer questions of interest in injection seeding, such as the tolerance for detuning of the seed light from a cavity mode, tolerance to phase mismatch in the crystal, comparison of seeding with cw and pulsed light, the influence of the pump pulse's temporal shape and energy; and the role of pump bandwidth in seeding. A general model to address these issues should permit multimode pump light, arbitrary mirror reflectivities, a realistic quantum-noise model, arbitrary seed-light properties, frequency-selective cavity elements, and variable crystal properties. As we will show, our models meet these criteria.

We have chosen the OPO diagrammed in Fig. 1 as the target for our models, although the extension to other configurations is straightforward. The model must inte-
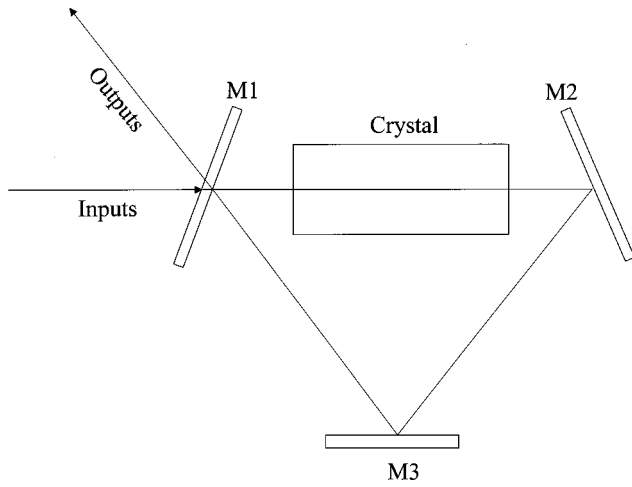
Fig. 1.   Diagram of the optical parametric oscillators modeled in this paper.   The reflectivities of mirrors M2 and M3 are 1.0 for all three waves.   Mirror M1 reflectivities and other parameters are given in Tables 1 and 2.

grate the signal, idler, and pump wave equations through the crystal including nonlinear source terms, and it must apply appropriate boundary conditions at the mirrors and crystal interfaces.

We define the signal field in terms of a carrier frequency ω_s by

$$
E_s(t,z) = \frac{1}{2}\{\epsilon_s(t,z)\exp[-i(\omega_s t - k_s z)]
$$

$$
+ \epsilon_s^*(t,z)\exp[i(\omega_s t - k_s z)]\}, \qquad (1)
$$

so temporal and spatial structure is described by the coefficient $\epsilon_s(t,z)$.   Outside the crystal $k_s = \omega_s/c$, and inside the crystal $k_s = n_s\omega_s/c$, where n_s is the crystal index of refraction at the signal wavelength.   Similar relations describe the idler and the pump waves.   The boundary conditions simply require that at the input mirror the field amplitudes of the output waves are the sum of reflected input and transmitted circulating field amplitudes,

$$
\epsilon_j^{\text{out}}(t, z = 0) = \sqrt{1 - R_j}\,\epsilon_j^{\text{circ}}(t, z = L)\exp(i\phi_j)
$$

$$
- \sqrt{R_j}\,\epsilon_j^{\text{in}}(t, z = 0), \qquad (2)
$$

and the circulating amplitudes are the combination of the transmitted input amplitudes and the reflected circulating amplitudes

$$
\epsilon_j^{\text{circ}}(t, z = 0) = \sqrt{1 - R_j}\,\epsilon_j^{\text{in}}(t, z = 0)
$$

$$
+ \sqrt{R_j}\,\epsilon_j^{\text{circ}}(t, z = L)\exp(i\phi_j), \qquad (3)
$$

where $j = s, i, p$ for signal, idler, or pump, and the R_j's are the reflectivities of the input mirror.   The cavity round-trip length is L, and z values 0 and L refer to positions just after and just before the input mirror.   The phases ϕ_j are residual round-trip phases proportional to the detuning of the carrier waves from cavity resonance. At the crystal input face the field in the crystal is related to the circulating field by

$$
\epsilon_j(t, z = z_{\text{in}}) = \sqrt{\frac{1 - R_j^{\text{in}}}{n_j}}\,\epsilon_j^{\text{circ}}(t, z = z_{\text{in}}), \qquad (4)
$$

and at the exit face the relation is

$$
\epsilon_j^{\text{circ}}(t, z = z_{\text{out}}) = \sqrt{(1 - R_j^{\text{out}})n_j}\,\epsilon_j(t, z = z_{\text{out}}). \qquad (5)
$$

The three-wave parametric mixing equations that must be integrated inside the crystal are well known[3] to reduce in the plane-wave limit to

$$
\left(\frac{\partial}{\partial z} + \frac{1}{v_s}\frac{\partial}{\partial t} + i\alpha_s\frac{\partial^2}{\partial t^2}\right)\epsilon_s(t,z)
$$

$$
= \frac{i\omega_s d_{\text{eff}}}{n_s c}\epsilon_p(t,z)\epsilon_i^*(t,z)\exp(i\Delta k z) \equiv P_s(t,z), \quad (6)
$$

$$
\left(\frac{\partial}{\partial z} + \frac{1}{v_i}\frac{\partial}{\partial t} + i\alpha_i\frac{\partial^2}{\partial t^2}\right)\epsilon_i(t,z)
$$

$$
= \frac{i\omega_i d_{\text{eff}}}{n_i c}\epsilon_p(t,z)\epsilon_s^*(t,z)\exp(i\Delta k z) \equiv P_i(t,z), \quad (7)
$$

$$
\left(\frac{\partial}{\partial z} + \frac{1}{v_p}\frac{\partial}{\partial t} + i\alpha_p\frac{\partial^2}{\partial t^2}\right)\epsilon_p(t,z)
$$

$$
= \frac{i\omega_p d_{\text{eff}}}{n_p c}\epsilon_i(t,z)\epsilon_s(t,z)\exp(-i\Delta k z) \equiv P_p(t,z), \quad (8)
$$

where Δk is the phase-velocity mismatch for the carrier waves defined by

$$
\Delta k = k_p - k_s - k_i, \qquad (9)
$$

and the carrier frequencies satisfy

$$
\omega_p = \omega_s + \omega_i. \qquad (10)
$$

The second terms on the left in Eqs. (6)–(8) are associated with the group velocity, v, of each wave, defined by

$$
\frac{1}{v} = \frac{n}{c} + \frac{\omega}{c}\frac{\mathrm{d}n}{\mathrm{d}\omega} = \frac{\mathrm{d}k}{\mathrm{d}\omega}. \qquad (11)
$$

The third term describes group-velocity dispersion and is usually important only for bandwidths greater than several hundred wave numbers.   Because this is seldom the case for nanosecond OPO's, except near degeneracy for type 1 mixing, we disregard that term throughout this paper.

In our previous model of single-longitudinal-mode OPO's, we ignored group-velocity differences among the three waves, in effect assuming that all three waves propagate with equal group velocity.   This was appropriate for near-monochromatic operation, where the time structure on the optical fields was limited to a scale much longer than any of the group-velocity walk-off times defined by

$$
\tau_{jk} = L_c\left(\frac{1}{v_j} - \frac{1}{v_k}\right), \qquad (12)
$$

where L_c is the crystal length.   For a broad-bandwidth OPO, in contrast, the waves are structured on a time scale as short as the signal–idler walk-off time, τ_{si}, so the group-velocity terms must be retained.   In fact, it is the time slippage between the signal and the idler waves ow-

ing to their differing group velocities that is responsible for smoothing structure over times shorter than τ_{si}, limiting the operating bandwidth of a free-running OPO to about τ_{si}^{-1} or less. Our new models integrate Eqs. (6)–(8), retaining the group-velocity term.

There are a few published theoretical treatments of multimode OPO's.[4–9] However, most neglect the group-velocity term, and consequently they provide a poor physical description of broad-bandwidth OPO's, although in some cases they predict spectral bandwidths reasonably well. Several of the models[4–7] are based on an early theory of OPO's by Yariv and Louisell.[10] This analysis starts with three coupled first-order equations of motion for longitudinally space-averaged field amplitudes derived by expanding the intracavity signal, idler, and pump fields in a set of lossless and orthonormal cavity modes. The resulting rate equations are supposed to describe the time development of these fields in the case of single-mode operation with a single-mode pump. Cassedy and Jain,[4] Kong *et al.*,[5] Schroder *et al.*,[6] and Boller and Schroder[7] adapted these rate equations to the case of multiple signal and idler modes, assuming a single pump mode. However, it has been shown by numerous experiments and models[1,11,12] that the assumption of spatially uniform fields is violated for most nanosecond OPO's. Generally, the pump beam is not resonated and is severely depleted as it passes through the crystal. Additionally, the idler wave is often unresonated and must grow from zero at the input end of the crystal to its output value. Even the resonated signal wave is nonuniform because the output coupling in nanosecond OPO's is high, typically 0.1 to 0.5. To allow for nonuniform fields, Fix and Wallenstein[8] modified this approach by using the mixing equations above without the group-velocity terms. A single-mode pump was assumed, but N pairs of signal and idler modes were allowed with a value of Δk assigned to each pair. The $(2N + 1)$ equations corresponding to Eqs. (6)–(8) above were integrated in z, assuming equal group velocities for all waves, and applying the boundary conditions at the mirrors on each round trip of the cavity. One problem with this method is that it does not properly handle group-velocity effects. The Δk's appear only in the nonlinear polarization terms and describe the phase adjustments from nonlinear mixing but not those from linear propagation. All temporal structure that develops on the pulses is assumed to propagate with the same velocity for the three waves rather than with their actual group velocities. This method has been successful in predicting the linewidths of unseeded nanosecond OPO's, but a more realistic model that includes group-velocity differences is needed to describe accurately the full range of broadband OPO behavior, including the effects of injection seeding. Only the model recently presented by Arisholm[9] includes the group velocities. He uses two different approximate methods of treating them, with the more accurate method based on shifting a field by one time-resolution step when its accumulated walk-off equals one time step.

In contrast to Fix and Wallenstein,[8] we follow the time development of only three waves, the carrier waves for the signal, the idler, and the pump. Spectra are deduced from the time-dependent structure that develops on these waves. Generally, the structure will be nearly periodic with a cavity round-trip repetition time, corresponding to the usual longitudinal cavity modes. The time structure will be smoothed over a time scale of t_{si}, the signal/idler walk-off time, limiting the spectral width to the crystal's acceptance bandwidth or less. Using this approach, Eqs. (6)–(8), including the group-velocity term, have successfully described single-pass parametric mixing of broad-bandwidth pulses[13–21] as well as synchronously pumped OPO's.[22,23] Two common methods of numerical solution are the Runge–Kutta direct integration method as outlined by Bakker *et al.*,[13] and the split-step integration method in which linear propagation steps are alternated with nonlinear mixing steps. We present two examples of the latter method. We also present a method of solution based on the exact cavity equations of motion, which are derived by expansion of the fields in a Fourier series of longitudinal modes. Our mode-expansion formulation allows for spatially nonuniform fields, arbitrary mirror reflectivities, and group-velocity mismatch. All three models described below give identical results for simulating broadband OPO's in the plane-wave limit.

2. SPLIT-STEP METHOD 1

In our first implementation of the split-step method, the field $\epsilon_j(t, z + \Delta z)$ is determined from $\epsilon_j(t, z)$ first by integration of the equations without the nonlinear source term. In a reference frame with time transformed to keep the pulse with the fastest group velocity, v_m, stationary in time, defined by

$$z' = z, \tag{13}$$

$$t' = t - z/v_m, \tag{14}$$

the propagation equations inside the crystal have the form

$$\left[\frac{\partial}{\partial z} + \left(\frac{1}{v_j} - \frac{1}{v_m} \right) \frac{\partial}{\partial t'} \right] \epsilon_j(t', z) = 0. \tag{15}$$

Fourier transforming from t' to ω converts this equation to

$$\left[\frac{\partial}{\partial z} + i \Delta \omega_j \left(\frac{1}{v_j} - \frac{1}{v_m} \right) \right] \epsilon_j(\Delta \omega_j, z) = 0, \tag{16}$$

where

$$\epsilon_j(\Delta \omega_j, z) = \int_{-\infty}^{\infty} \epsilon_j(t', z) \exp(i \Delta \omega_j t') \mathrm{d}t', \tag{17}$$

and $\Delta \omega_j$ is the detuning of the Fourier wave from its carrier frequency. Equation (16) shows that linear propagation over step Δz in $\{\Delta \omega_j, z\}$ space is equivalent to shifting the phase of each monochromatic wave of frequency shift $\Delta \omega_j$ by $[\Delta z \Delta \omega_j (1/v_j - 1/v_m)]$, so linear propagation is handled by transforming to $\{\Delta \omega, z\}$ space, shifting the phase of each monochromatic wave as indicated, and transforming back to $\{t', z\}$ space. The nonlinear mixing half-step is then performed in $\{t', z\}$ space by integration of the mixing equations without the group-velocity term

$$\frac{\partial}{\partial z} \epsilon_j(t', z) = P_j(t', z) \qquad (18)$$

over the step Δz, with a Runge–Kutta method.

Figure 2 illustrates the details of our implementation. The input fields $\epsilon_j^{\text{in}}(t)$ are specified gridded in time. They are modified by the input mirror and input face reflections to give the fields just inside the crystal input face $\epsilon_j(t, z_0)$. As we just described, these fields are Fourier transformed from $\{t, z_0\}$ to $\{\Delta\omega, z_0\}$, the phase shifts are applied, and the fields are transformed back to $\{t, z_0\}$ space. The use of the transformed time t' is a convenience to keep the pulses nearly centered in the time grid. The mixing step then modifies the fields at each point of the time grid according to Eq. (18), giving $\epsilon_j(t, z_1)$. This process is repeated until the final z step in the crystal is reached. The fields exiting the crystal are then delayed on the time grid by the round-trip time of the fastest wave, t_m^{rt}, and split into components reflected and transmitted by the input mirror. The reflected components are added to the transmitted components of the original input fields, and the resulting fields are again passed through the crystal, giving results accurate for two crystal passes or over the time interval $(0 - 2t_m^{\text{rt}})$. This process is repeated for a third pass, giving results accurate over $(0 - 3t_m^{\text{rt}})$ and so on until the entire pulse duration is modeled.

We have verified that this method works. However, it is computationally inefficient because the entire time range of the pulses is propagated through the crystal to extend the time history of the pulses by only t_m^{rt}, requiring many passes with large time arrays. A much more efficient method is to propagate only one round-trip time slice per pass. To find the starting fields for pass N, the reflected light from pass $(N - 1)$ is combined with the Nth slice of transmitted input light, and the entire history is built up one pass at a time. In practice, we use time slices somewhat longer than a single round-trip time, specifying the field over the interval $[(N - 1)t_m^{\text{rt}} - \Delta t]$ to $(Nt_m^{\text{rt}} + \Delta t)$. This is necessary because group-velocity differences make the round-trip times different for the three waves. We use the round-trip time of the fastest wave as the nominal round-trip time. Propagation of the slower waves causes light from one round-trip slice to flow into the next, so a portion of the preceding slice must be included to accommodate this flow. Additional extra time is used to prevent aliasing in the Fourier
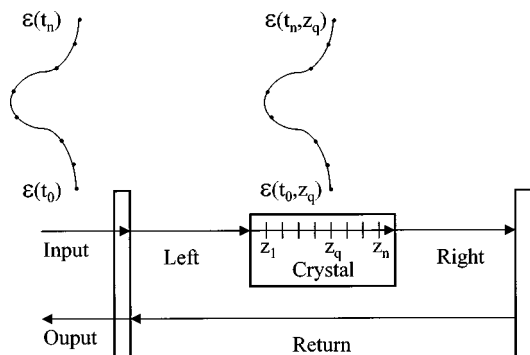

Fig. 2. Example of OPO model gridding for split-step method 1. The pulses are gridded in time at each z point.

Table 1. Parameters of Example OPO

Parameter	Pump	Signal	Idler
Wavelength (nm)	355	710	710
Refractive index	2.2	2.2	2.2
Group-velocity index	2.275	2.2	2.35
Crystal absorption (cm^{-1})	0	0	0
Input energy (J)	0.4	quantum noise + variable seed	quantum noise
FWHM pulse duration (ns)	2		
FWHM beam diameter (mm)	4	4	4
Input mirror reflectivity	0	0.7	0
Cavity length (mm)	11	Crystal length (mm)	5
d_{eff} (pm/V)	2	Δk (mm^{-1})	0

transform. This extra interval is usually ~20 time points, and we weight them so the field amplitudes smoothly drop from actual amplitudes at the splice point to zero at the end points. At the end of each round-trip calculation, the spliced-on time zones are dropped, and the remaining field is the calculated field for the Nth pass of the cavity. This method assumes that light in the Nth time slice is unaffected by light outside the included time interval, a good approximation so long as there are no sharp features in the spectral response of the crystal that would have a corresponding time transform longer than Δt. This requirement is almost always met with nonlinear crystals of interest in OPO applications, and is essentially the same assumption made in dropping higher-order time-derivative terms (group-velocity dispersion and higher-order dispersion terms) in the mixing equations.

Frequency-selective intracavity elements such as etalons can be accommodated in this method even though they might have narrow spectral structure. Reflections within an etalon will introduce time delays that cause some of the light from one OPO round-trip time slice to overflow into later slices. This can be handled by passing the fields covering the full currently known time range from $t = 0$ to $t = Nt_m^{\text{rt}}$ through the intracavity element on each pass. Two copies of the fields must be kept, one that has been modified by the element and one that has not. The former is used in the crystal calculations; the latter is passed through the intracavity element to find the new time history after each pass of the cavity.

To illustrate this method, we modeled the OPO of Fig. 1, using the operating parameters listed in Table 1. As a starting point we create an input time grid, dimensioned identically for all three waves, with a time step adjusted to resolve the full acceptance bandwidth of the crystal, and a length sufficient to contain the full duration of the input and the output pulses. We fill this grid with the applied pump, signal, and idler fields. The signal and the idler fields include quantum noise in addition to any seed light. Quantum noise is simulated by filling each longitudinal, or frequency, mode of the input grid with

light of random phase and with Gaussian amplitude distribution normalized to an average of one half photon per longitudinal mode. A random-number generator assigns the phases over the range $0–2\pi$, and the amplitudes are created by translation of a separate set of random numbers to a Gaussian distribution. Enough modes are filled so the spectrum spans the full acceptance bandwidth of the crystal, and they are centered on the carrier frequency of the signal or idler. These fields are Fourier transformed to the time domain and inserted in the input grid. This gives a Gaussian field amplitude distribution at the input mirror with a correlation time less than the inverse crystal acceptance bandwidth. This treatment of quantum noise is similar to that of Arisholm.[9] Usually, broad-bandwidth OPO's have linewidths three to five times smaller than the crystal acceptance bandwidth, so starting with a noise spectrum slightly broader than the acceptance bandwidth should avoid artificial narrowing of the output spectrum. The time spanned by the input grid is a few times the duration of the pump pulse, which in turn is many times the cavity round-trip time, forcing the frequency spacing of the noise modes to be much less than the cavity mode spacing. In this model, the cavity boundary conditions and the crystal gain select the oscillating modes; we make no assumptions about them. We do assume that we are modeling the central rays of lowest-order Gaussian transverse modes of specified diameters. This should be realistic for low-Fresnel-number OPO's that support oscillation on only a single transverse mode.

3. SPLIT-STEP METHOD 2

The second model is also based on split-step integration, but rather than transforming between t and ω, we transform between z and k_z in the propagation half of the split step. This propagates the fields over equal t steps rather than over equal z steps. In a reference frame with z transformed so the fastest-moving pulse is stationary in z', defined by

$$z' = z - v_m t, \qquad (19)$$

$$t' = t, \qquad (20)$$

the propagation equations take the form

$$\left[(v_j - v_m)\frac{\partial}{\partial z'} + \frac{\partial}{\partial t} \right] \epsilon_j(t, z') = 0. \qquad (21)$$

In $\{t, k_z\}$ space they take the form

$$\left[i(v_j - v_m)\Delta k_z + \frac{\partial}{\partial t} \right] \epsilon_j(t, \Delta k_z) = 0. \qquad (22)$$

A z grid is set up in the crystal. We define a time step, Δt, as the time for the fastest wave to move one z step. Grids with this time step are set up outside the crystal as shown in Fig. 3. The input fields are placed on the input grid with time proceeding right to left as shown. Each step in the integration will represent a time snapshot of the fields. Propagation in the crystal proceeds by Fourier transforming all but the fastest wave from $\{t, z'\}$ to $\{t, k_z\}$ over the full crystal length, phase shifting each monochromatic wave by $[\Delta k_z \Delta t (v_i - v_m)]$ and trans-
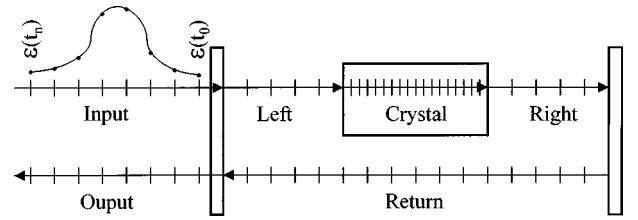

Fig. 3. Example of OPO model gridding for split-step method 2. The z grids outside the crystal are spaced by $\Delta z = c\Delta t$; that inside the crystal is spaced by $\Delta z = v_m \Delta t$, where v_m is the fastest of the three group velocities.

forming back to $\{t, z'\}$. Here, Δk_z is the offset from the wave vector of the associated carrier wave. This shifts the slower waves to the left, or toward smaller z', by the amount $[\Delta t(v_m - v_i)]$, a small fraction of the grid interval. All the fields are then clocked one grid space clockwise over the full cavity and input and output grids, applying the mirror and crystal transmission and reflection coefficients to satisfy boundary conditions. The propagation transform is performed only over the crystal length, rather than over the full cavity. As before, we justify this by noting that ordinarily it is only the light within the crystal that determines the propagation in the crystal. Buffer zones are appended to the crystal fields similar to those described for method 1 above to avoid aliasing in the fast Fourier transforms.

The mixing half of the split step consists of integrating Eqs. (6)–(8) from t_0 to $(t_0 + \Delta t)$, neglecting the propagation term. The mixing equations of form

$$\frac{\partial}{\partial t} \epsilon_j(t, z') = v_j P_j(t, z') \qquad (23)$$

are integrated at each grid point within the crystal. We applied this method under identical conditions to the example above and achieve results identical to those of method 1.

It is possible to include intracavity etalons in this method directly by adding the etalon-mirror reflective boundary conditions to the grid propagation. This is straightforward if the etalon mirrors lie on grid points. If not, fast-Fourier-transform methods can be used to shift fields a fraction of a grid spacing to simulate the etalon accurately.

4. CAVITY-MODE-EXPANSION METHOD

The cavity-mode expansion method derives exact cavity equations of motion for the intracavity fields by expanding each field in terms of the longitudinal spatial modes of the OPO cavity. This approach has been successfully applied to lasers with externally injected fields.[24] The key step in expanding the fields in a Fourier series of longitudinal modes is to write the field amplitudes inside the cavity as

$$\epsilon_j(t, z) = A_j(t, z)u_j(z)\gamma_j \exp\left[-\frac{z}{L}\ln(\gamma_j) \right] + \epsilon_j^{\text{inj}}(t, z). \qquad (24)$$

The motivation for this expansion is to define amplitudes $A_j(t, z)$ that are continuous throughout the cavity and

satisfy periodic boundary conditions at $z = 0$ and $z = L$ so Fourier transforms can be used. The functions $u_j(z)$ satisfy

$$\frac{\mathrm{d}u_j(z)}{\mathrm{d}z} = 0 \qquad (25)$$

inside and outside the crystal except at the crystal faces and mirrors, where they are discontinuous. They satisfy all boundary conditions at discrete locations in the cavity (mirror reflections, crystal surface losses, and phase shifts upon reflection and transmission at surfaces). Because all the discontinuous boundary conditions inside the cavity are handled by the functions $u_j(z)$, the amplitudes $A_j(t, z)$ are continuous between $0 < z < L$. At the input mirror the functions $u_j(z)$ satisfy the reduced boundary condition

$$\sqrt{R_j} \exp(i\omega_j L/c) u_j(L) = \gamma_j u_j(0). \qquad (26)$$

The eigenvalues γ_j are found from the solution of Eq. (26) to be

$$\gamma_j = \sqrt{R_j} \sqrt{1 - R_j^{\mathrm{out}}} \sqrt{1 - R_j^{\mathrm{in}}} \exp(i\phi_j), \qquad (27)$$

with ϕ_j being the residual round-trip phase caused by detuning of the carrier from cavity resonance. Thus the functions $u_j(z)$ and the constants γ_j handle discontinuities in the cavity fields for arbitrary mirror reflectivities, crystal reflectivities, and cavity detunings.

In order to make the $A_j(t, z)$'s periodic, it is also necessary to factor out the injected fields as in Eq. (24). These are the fields that develop in the passive cavity owing to the input fields so they satisfy the homogeneous plane-wave equation (no nonlinear polarization term) with boundary conditions

$$\epsilon_j^{\mathrm{inj}}(t, 0) = \sqrt{1 - R_j}\epsilon_j^{\mathrm{in}}(t) + \sqrt{R_j}\epsilon_j^{\mathrm{inj}}(t, L)\exp(i\phi_j). \qquad (28)$$

Analytical expressions for $\epsilon_j^{\mathrm{inj}}(t, z)$ are easily obtained for the OPO cavity shown in Fig. 1. Substituting Eq. (24) into the mixing equations, we find the amplitudes $A_j(t, z)$ satisfy

$$\left(\frac{\partial}{\partial z} + \frac{1}{v_j}\frac{\partial}{\partial t} - \frac{1}{L}\ln\gamma_j\right)A_j(t, z) = \frac{P_j(t, z)}{\gamma_j u_j(z)\exp(-z\ln\gamma_j/L)} \qquad (29)$$

throughout the cavity, where $v_j(z)$ is v_j in the crystal and c in air. By use of Eqs. (26) and (28), the $A_j(t, z)$'s satisfy the periodic boundary conditions

$$A_j(t, 0) = A_j(t, L) \qquad (30)$$

at all times. Because they are also continuous functions of z, they can be expanded in a Fourier series of longitudinal modes of the empty ring cavity

$$A_j(t, z) = \sum_q A_q^j(t)\exp(-i2\pi qz/L), \qquad (31)$$

where q is the cavity mode integer. The expansion coefficients evolve in time according to

$$\frac{\mathrm{d}A_{q'}^j(t)}{\mathrm{d}t} = \frac{1}{L}\sum_q V_{q',q}^j A_q^j(t)(\ln\gamma_j + i2\pi q)$$

$$+ \frac{1}{L}\int_0^L \mathrm{d}z\,\frac{v_j(z)P_j(t, z)}{\gamma_j u_j(z)}$$

$$\times \exp\left(\frac{z}{L}\ln\gamma_j + i2\pi q'\frac{z}{L}\right), \qquad (32)$$

where

$$V_{q,q'}^j = \frac{1}{L}\int_0^L \mathrm{d}z\,v_j(z)\exp\left[i2\pi(q' - q)\frac{z}{L}\right]. \qquad (33)$$

Equation (32) represents the coupled equation of motion for each Fourier component of each field inside the OPO cavity. We solved these equations under identical conditions to the example above and achieved results identical to those of methods 1 and 2. This gives us confidence that all three methods correctly solve the three-wave mixing equations with group-velocity differences subject to the OPO cavity boundary conditions.

Including intracavity etalons is not straightforward in this formulation. In principle, one could find the longitudinal modes of the OPO cavity with an etalon in the cavity, and then expand the fields in terms of these modes. However, methods 1 and 2 offer a much more straightforward approach for including etalons. Finally, transverse effects can be included by expansion of the fields in the transverse modes of the bare cavity.

5. COMPARISON OF METHODS

Each of our models has its strengths and weaknesses. For a direct comparison among them, we chose the example of Table 1. For method 1 the time step was 0.303 ps, the number of time steps included in each single-pass integration was 256, and the number of z steps in the crystal was 50. Run time was ~5 min on a 300-MHz Pentium II computer with the simulation programmed in APL, an interpreted language. For FORTRAN or C++ implementations, the run time would probably be halved. For method 2, the time step was 0.188 ps and the number of z grid points in the crystal was 256. Run time was slightly longer at ~15 min. The modeled OPO performance was identical for the two methods. The two run times should each scale approximately the same with changes in bandwidth, pulse duration, and crystal and cavity length, so there is not a clear winner in computation speed or memory requirements. Both can be readily extended to include diffraction and birefringent walk-off by inclusion in the propagation half-step of the transform from $\{x, y\}$ to $\{k_x, k_y\}$. Diffraction and walk-off are handled by addition of the diffractive and walk-off phase shifts, followed by transformation back to $\{x, y\}$.[25] This should apply equally to both split-step methods. This combination of group-velocity walk-off with diffraction and birefringent walk-off has been demonstrated by Milonni *et al.*[19] in a model of single-pass second-harmonic generation that uses the $(t \leftrightarrow \omega)$ transform method to handle group velocity. Arisholm[9] also combines this

treatment of diffraction with an approximate handling of group-velocity walk-off in his OPO model.

If the group-velocity dispersion terms in Eqs. (6)–(8) are important, for example, in a degenerate type 1 OPO, method 1 has an advantage because the nonlinear mixing equation remains a first-order equation, whereas in method 2 it becomes second order. One attractive feature of method 2 is that it gives a series of snapshots of the fields permitting a movielike display of the fields as they propagate through the crystal. This can provide valuable insight into the evolution of the mixing fields. Another advantage of method 2 is that it easily accommodates different cavity lengths for the signal and the idler in doubly resonant OPO's. The cavity grid external to the crystal is simply increased or decreased in size to lengthen or shorten the cavity. Implementations of these two methods are included in the public domain software package SNLO.[26]

The cavity mode expansion method is much slower than the other two, with a run time of ~2 h in FORTRAN. The reason for this is not clear, and we did not pursue this method further since methods 1 and 2 give identical results and run much faster. We speculate that one reason method 3 may be slow is because the pump and idler are not resonant in the example calculation yet they are expanded in OPO cavity modes. The expansion coefficients seem to vary rapidly in time, which requires small time steps and higher-accuracy integration schemes. We used a fourth-order Runge–Kutta scheme to solve the coupled equations Eq. (32) using a time step of 0.076 ps, 127 longitudinal modes, and 120 z-grid points in the crystal for the example of Table 1. Method 3 is of interest primarily as an extension of previous models of multimode lasers and OPO's, showing how they can be adapted to correctly model nanosecond OPO's.

6. EXAMPLE RESULTS AND DISCUSSION

In a pair of earlier papers,[1,2] we presented detailed laboratory measurements of the behavior of two similar KTP ring OPO's. We reported the unseeded linewidths, seed power threshold, and a set of measurements that indicated that the unseeded spectrum was nearly phase modulated with little amplitude modulation (AM). It is interesting to compare the predictions of our new models with these observations. The parameters for the KTP OPO are listed in Table 2. First, we consider the unseeded spectra. The model predicts large pulse-to-pulse variation in the signal and idler spectra, which reflects the variation in the start-up noise. Figure 4 shows two calculated unseeded spectra under identical operating conditions except for different signal and idler quantum noise. This large variation is in qualitative agreement with our laboratory observations. Figure 4 also shows the signal spectrum averaged over ten pulses. The averaged linewidth is ~2.5 cm^{-1}, in good agreement with the measured linewidth of ~3 cm^{-1}. In these runs the linewidth of the start up noise was 15 cm^{-1}. When cw seed light at the signal wavelength is added, the spectrum narrows as expected. Figure 5 shows a series of spectra corresponding to seed levels of 0, 1, 10, and 100 nW for the same starting noise in each case. There is slight narrow-

ing with 1 nW, but for 10 nW the seeded mode is ~100 times the strength of the other modes, and for 100 nW the seeded mode is ~1000 times the strength of the other modes. The seed light was exactly resonant with a cavity mode. This observation of a seeding threshold power of ~10 nW agrees with our measured seeding threshold[1] of ~10 nW.

The situation regarding mode correlation or phase modulation is more complex. In our earlier paper we presented a number of measurements that, taken together, indicated the light from the KTP OPO was nearly purely phase modulated, although there was no single definitive measurement. We measured directly the signal-wave AM at frequencies of less than 5 GHz, using a fast

Table 2. Parameters of KTP Ring OPO

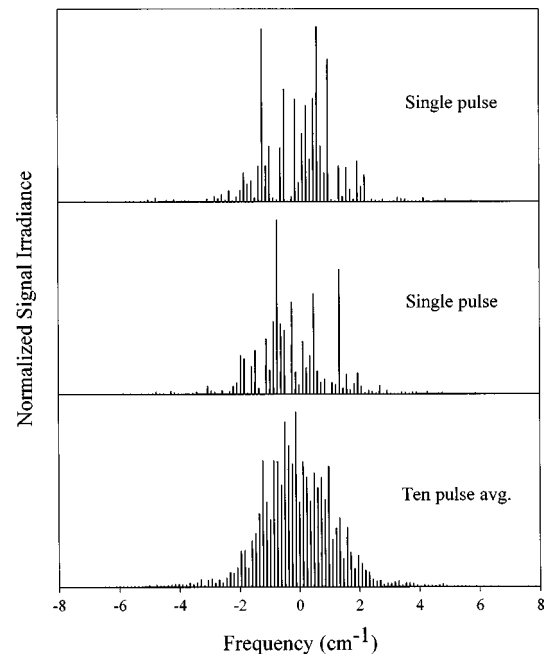| Parameter	Pump	Signal	Idler
Wavelength (nm)	532	800	1588
Refractive index	1.79	1.818	1.736
Group-velocity index	1.911	1.875	1.765
Crystal absorption (cm^{-1})	0	0	0
Input energy (J)	0.004	quantum noise + variable seed	quantum noise
FWHM pulse duration (ns)	7		
FWHM beam diameter (mm)	0.6	0.6	0.6
Input mirror reflectivity	0	0.84	0
Cavity length (mm)	73	Crystal length (mm)	10
d_{eff} (pm/V)	3.1	Δk (mm^{-1})	0

Fig. 4. Signal spectra for OPO of Table 2 pumped at twice threshold. The top two traces are for individual pulses with different start-up noise. The bottom trace is the average of ten pulses with fluctuating start-up noise. The averaged spectral width is ~2.5 cm^{-1} compared with the crystal acceptance bandwidth of 8 cm^{-1}.
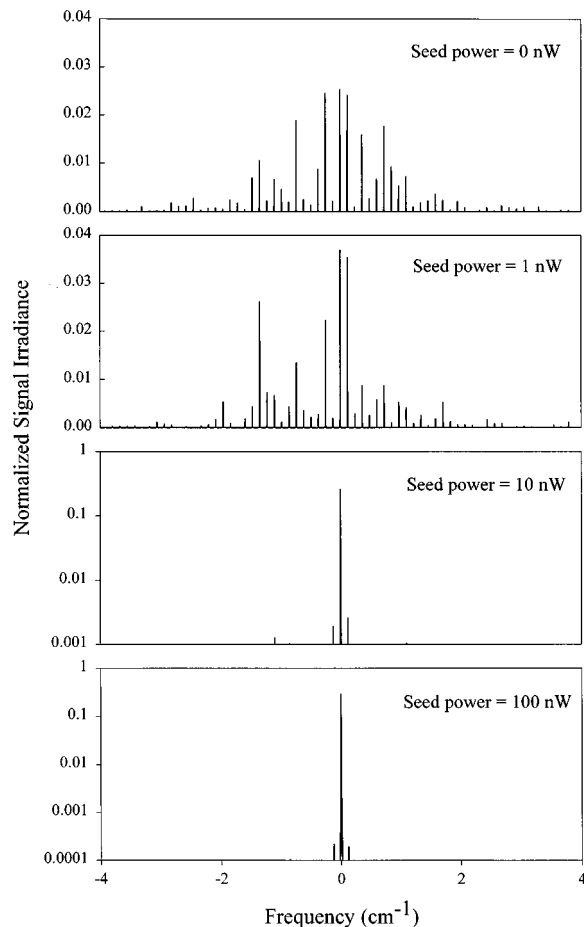
Fig. 5. Signal spectra for OPO of Table 2 pumped at twice threshold. The cw seed power incident on the input mirror is varied from 0 to 100 nW with the same start-up noise for each pulse. The spectra are normalized, so the sum of the energy in all modes is unity. Note the scale changes between the graphs.

oscilloscope and detector. This resolved only the 3.66-GHz adjacent mode beating. We found significant AM for pump levels near threshold, but it disappeared as the pump level was increased to two and three times threshold. We also summed the signal and the idler waves in a mixing crystal to create light at the pump wavelength. With no delay between the signal and the idler pulses, the reconstructed pump light was nearly monochromatic, but with a delay it developed sidebands. This indicated that the signal and the idler waves had large conjugate-phase excursions but relatively little AM. We also frequency doubled the signal wave, comparing doubling efficiency with and without injection seeding. The efficiency changed by 3% or less, indicating that the output signal light had much less AM than the quantum noise from which oscillation builds. From this experimental evidence we conclude that, unlike many Q-switched lasers, an OPO does not amplify the starting noise with weak correlations between modes to give nearly chaotic light, but rather produces light in several longitudinal modes with strong intermode correlations. The light behaves more like phase-modulated than chaotic light. In our earlier paper, we also presented a model calculation that pointed toward pure phase-modulated light. The model started with two signal cavity modes seeded so the seed

had strong AM. We integrated the mixing equations without the group-velocity terms and found that the AM was strongly suppressed at high pump levels but not near threshold, in qualitative agreement with experiment. We have now applied our new models that include the group-velocity terms to address the question of the correlation between modes. Based on a limited number of model runs, we find strong suppression of AM in a signal-resonant OPO if the group velocity of the pump is midway between those of the signal and the idler. With increasing deviation from that value, the AM tends to grow. Interestingly, this optimum value corresponds to exact phase matching for frequency summing pairs of signal and idler sidebands with equal detuning from their carriers. That is, all processes satisfying $[(\Delta\omega_s = N\delta) + (\Delta\omega_i = N\delta) \rightarrow (\Delta\omega_p = +2N\delta)]$ are exactly phase matched, where δ is the mode spacing. Why this should suppress AM most effectively is not obvious. This case is illustrated in Fig. 6, which shows time profiles of the signal wave for various pump levels for the OPO conditions of Table 1. Each run uses the same starting noise. The suppression of AM with increasing pump is apparent. Further, the leading edge of the signal pulses retains some modulation even at the higher pump levels, qualitatively agreeing with our laboratory observations. The details of the leading-edge modulation reflect the modulation in the start-up noise fields and fluctuate from pulse to pulse if different starting noise is used.

However, in the KTP OPO's of our earlier papers, the pump group velocity is slower than both the signal and the idler velocities. Our model indicates that AM suppression is weaker here. In fact, rather than producing a smooth time profile, methods 1 and 2 both predict a smooth profile interrupted by amplitude excursions with the characteristic shape shown in Fig. 7. The location
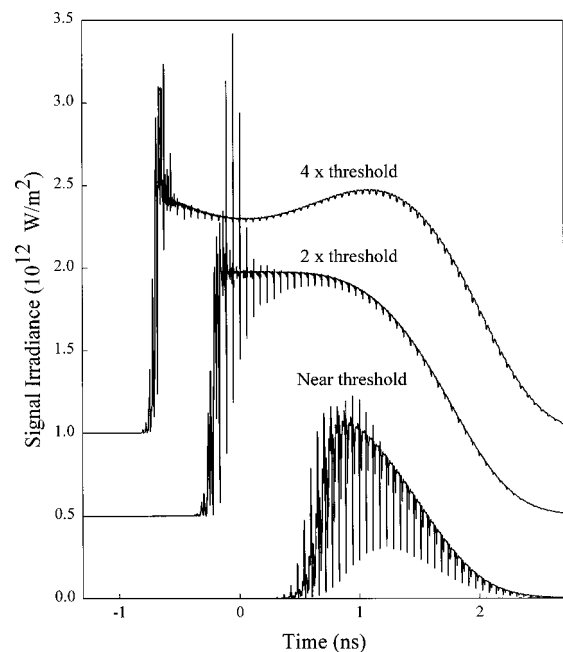

Fig. 6. Time profiles of the signal wave for the OPO of Table 1 with pump pulse fluences near threshold, twice threshold, and four times threshold. The pump pulse is centered a time zero and has a 7-ns width (FWHM).
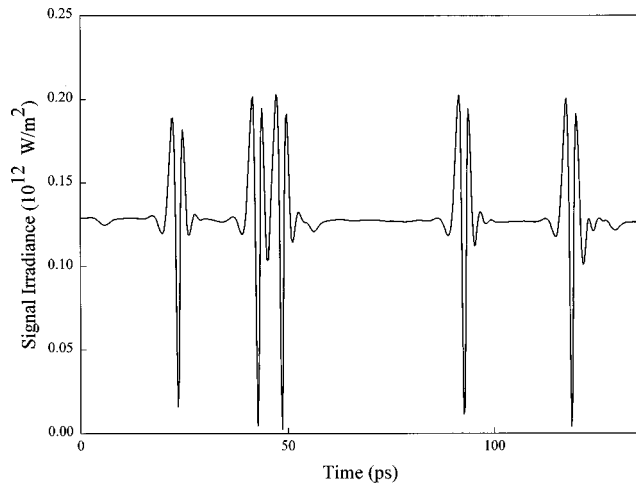
Fig. 7.   Time profile of the signal wave of the OPO of Table 2 pumped at twice threshold.   One half of a cavity round trip is displayed starting about midway through the signal pulse.

and abundance of these blips depends on the starting noise but their shape is nearly universal.   They persist for the duration of the pulse, recurring with a round-trip period.   They are a direct consequence of the difference in group velocities of the three waves, and their width approximates the pump/idler walk-off time τ_{ip} of 4.9 ps. Different sets of group velocities develop other characteristic shapes.   Interestingly, when we calculate the relative efficiency for frequency doubling the predicted signal wave, it is within 3% of a temporally smooth pulse, so the second-harmonic test of our previous work, which had a 3% detection limit, would not have clearly detected this type of AM.   Further, when we filter the signal wave as detected by a square-law detector to pass only frequencies <5 GHz, corresponding to our direct AM measurement, very little modulation appears on the pulse profile because the blips are bipolar with nearly equal positive and negative excursions.   Also, near threshold the characteristic shape is replaced by only negative excursions, so more AM is predicted.   This trend is in qualitative agreement with our earlier report.   However, as the pump level is increased to four times threshold, the number of blips increases, as does the 3.66-GHz AM, in disagreement with laboratory observations.   We must conclude that, while there is strong correlation between modes, perhaps AM suppression is not complete in all cases, including the KTP OPO's we studied.   We note, however, that a few percent idler feedback significantly reduced the number of blips.   Also, the velocity of the blips slows slightly with increasing pump level, so it may be that including realistic transverse beam profiles and diffraction would reduce or eliminate them.

   Not surprisingly, adding idler feedback to make the OPO of Table 2 doubly resonant dramatically alters this behavior.   As Arisholm notes,[9] the spectra narrow substantially for a doubly resonant OPO.   If we use $R_i = R_s = 0.4$ instead of $R_i = 0$, $R_s = 0.84$, the conversion efficiency is about the same but the signal and the idler spectra are narrowed by ~30% and AM is suppressed more strongly.   One factor acting to narrow the spectral width is the incommensurate mode spacings of the signal and the idler.   These are determined by the group veloci-

ties, so for equal cavity lengths the signal mode frequency spacing is ~1.4% less than the idler.   If the modes overlap at the carrier frequencies, they separate by 1.4% per mode of detuning.   Because the modes are quite narrow, this reduces the gain for modes detuned by ten or so modes, narrowing the spectrum slightly.   This effect can be exaggerated by further lengthening the signal cavity relative to the idler cavity.   This could be done with separate signal and idler mirrors.   Using method 2, which easily accommodates different cavity lengths for the two waves, we find that if the signal cavity is lengthened by ~4.5%, the spectrum is narrowed to almost a single mode. All detuned modes are suppressed below 5% of the central mode.   Weak modes occur in clusters separated from the central mode cluster by ~1.5 cm^{-1}.   This is similar to the cluster tuning effect commonly noted for cw OPO's.   The effect is akin to inserting a line-narrowing etalon in the OPO cavity.   However, this spectral narrowing is accompanied by increased high-frequency AM.   If we shorten the signal cavity so the mode spacings of the signal and the idler waves are matched, the AM suppression is enhanced compared with equal-length cavities, and the spectra are slightly broadened.   In fact, the AM suppression in this case is almost as strong as in the OPO of Table 1 and Fig. 6.

   Another testable feature predicted by our model is the existence of many low-level sidebands on the depleted pump light even though the input pump is single mode. A predicted power spectrum shown in Fig. 8 for the KTP ring OPO of Table 2 has many sidebands at the subpercent level spread over a range approximately equal to the 8-cm^{-1} crystal acceptance bandwidth, with peaks separated by the OPO mode spacing.   For seeded operation, these sidebands are absent.   We verified this behavior in a laboratory OPO by analyzing the depleted pump light using a Fabry–Perot etalon.   Figure 9 compares depleted pump spectra for seeded and unseeded operation along with a reference spectrum taken by blocking of the signal wave inside the OPO cavity to prevent oscillation.   Note the presence of many low-level modes only in the unseeded case.   Our analyzing Fabry–Perot had a free spectral range of 45.4 GHz and finesse of ~35.   We scanned the central spot of the etalon with each point on the trace
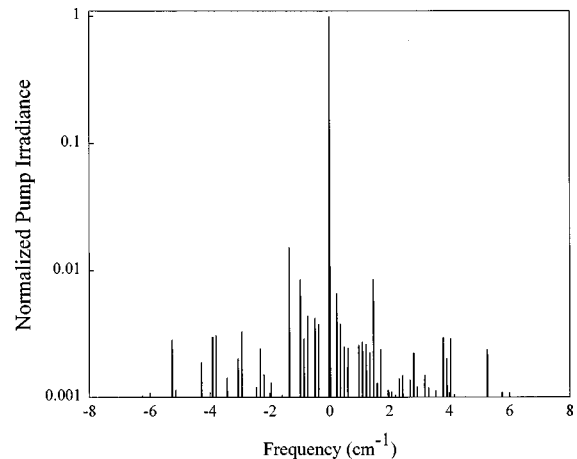

Fig. 8.   Computed spectrum of the depleted pump wave for the OPO of Table 2 pumped at twice threshold.
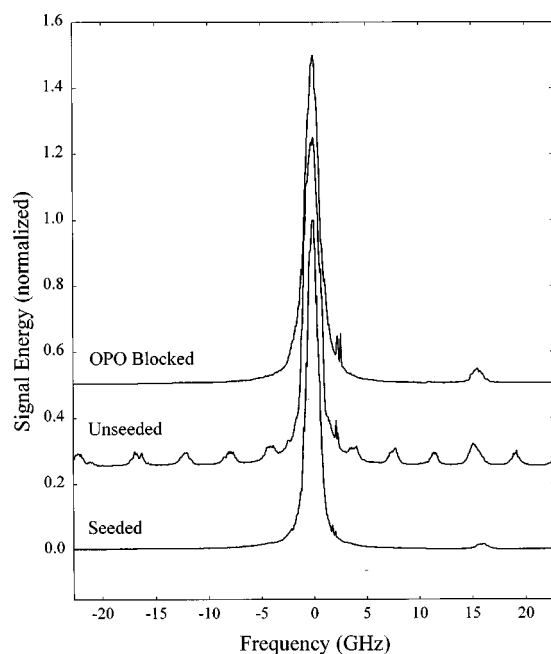
Fig. 9.   Measured spectra of the depleted pump wave for un-seeded (middle trace) and seeded (bottom trace) OPO of Table 2. The top trace is a reference trace with the signal path blocked inside the OPO cavity.   Each sideband is the overlap of side-bands from several etalon orders.   The etalon free spectral range is 45.4 GHz, and the OPO cavity free spectral range is 4.1 GHz.   The peaks at +2 and +14 GHz are measurement arti-facts.

representing the average over approximately ten pulses. The sidebands on the depleted pump extend beyond the free spectral range of the etalon, so each sideband is ac-tually a sum of sidebands associated with different etalon orders.   The etalon spacing was adjusted to overlap the orders.   From a separate etalon scan with the free spec-tral range extended to 6 cm^{-1}, we find that the sidebands extend at least 5 cm^{-1} on each side of the input pump fre-quency.   The individual sideband energies are in the range 0.3%–1%.

7.   CONCLUSIONS

We demonstrated three methods of modeling broad-bandwidth nanosecond OPO's in the plane-wave limit and show excellent agreement among them.   We pointed out the advantages and limitations of each and indicated how they could be modified to include diffraction and birefrin-gent walk-off as well as how intracavity frequency-selective elements could be included.   The models predict that unseeded OPO's generate light with unusual spectral properties.   It is broadband but has much less amplitude modulation than it would if random phases were assumed for the longitudinal modes.   Evidently the modal phases are locked in such a way that they produce nearly phase-modulated light, in accord with our earlier laboratory observations.[2]   We also find that the group velocity of the pump light relative to those of the signal and the idler has an impact on the spectral properties of an OPO.   With a pump velocity intermediate between signal and idler ve-locities, AM suppression is strongest.   Additionally, the output waves tend to develop characteristic blips whose

shape depend on the relative group velocities.   We expect these models will provide a guide in designing nanosec-ond OPO's with spectral control either by injection seed-ing or by use of intracavity frequency-selective elements. Although we have not presented examples here, our mod-els also permit the use of multimode pump light, so the influence of the pump spectrum can also be studied.   Fi-nally, we note that method 1 can readily accommodate group-velocity dispersion terms so it should be possible to model degenerate type 1 OPO's with their extremely large bandwidths.

ACKNOWLEDGMENTS

REFERENCES AND NOTES

1.   A. V. Smith, W. J. Alford, T. D. Raymond, and M. S. Bow-ers, "Comparison of a numerical model with measured per-formance of a seeded, nanosecond KTP optical parametric oscillator," J. Opt. Soc. Am. B **12**, 2253–2267 (1995).
2.   D. J. Armstrong and A. V. Smith, "Tendency of nanosecond optical parametric oscillators to produce purely phase-modulated light," Opt. Lett. **21**, 1634–1636 (1996).
3.   Y. R. Shen, *The Principles of Nonlinear Optics* (Wiley, New York, 1984).
4.   E. S. Cassedy and M. Jain, "A theoretical study of injection tuning of optical parametric oscillators," IEEE J. Quantum Electron. **QE-15**, 1290–1301 (1979).
5.   Y. Kong, Z. Xu, Y. Zhou, D. Deng, X. Zhu, and L. Wu, "The compound cavity optical parametric oscillator: theory and experiment," IEEE J. Quantum Electron. **34**, 439–446 (1998).
6.   T. Schroder, K.-J. Boller, A. Fix, and R. Wallenstein, "Spec-tral properties and numerical modeling of a critically phase-matched nanosecond LiB$_3$O$_5$ optical parametric oscil-lator," Appl. Phys. B: Photophys. Laser Chem. **58**, 425–438 (1994).
7.   K.-J. Boller and T. Schroder, "Demonstration of broadband intracavity spectroscopy in a pulsed optical parametric os-cillator made of β-barium borate," J. Opt. Soc. Am. B **10**, 1778–1784 (1993).
8.   A. Fix and R. Wallenstein, "Spectral properties of pulsed nanosecond optical parametric oscillators: experimental investigation and numerical analysis," J. Opt. Soc. Am. B **13**, 2484–2497 (1996).
9.   G. Arisholm, "Advanced numerical simulation models for second-order nonlinear interactions," Proc. SPIE **3685**, 86–97 (1999); G. Arisholm, "Quantum noise initiation and macroscopic fluctuations in optical parametric oscillators," J. Opt. Soc. Am. B **16**, 117–127 (1999).
10.   A. Yariv and W. H. Louisell, "Theory of the optical paramet-ric oscillator," IEEE J. Quantum Electron. **QE-2**, 418–424 (1966).
11.   T. Debuisschert, "Nanosecond optical parametric oscilla-tors," Quantum Semiclassic. Opt. **9**, 209–219 (1997).
12.   K. D. Shaw, "Spatio-temporal evolution of the intra-cavity fields in a pulsed doubly resonant optical parametric oscil-lator," Opt. Commun. **144**, 134–160 (1997).
13.   H. J. Bakker, P. C. M. Planken, and H. G. Muller, "Numeri-cal calculation of optical frequency-conversion processes: a new approach," J. Opt. Soc. Am. B **6**, 1665–1672 (1989).
14.   M. Cavallari, G. M. Gale, F. Hache, L. I. Pavlov, and E. Rousseau, "Mid infra-red femtosecond pulse generation by wave-mixing: numerical simulation an experiment," Opt. Commun. **114**, 329–332 (1995).

15. R. Danielius, A. Dubietis, A. Piskarskas, G. Valiulis, and A. Varanavicius, "Generation of compressed 600–720-nm tunable femtosecond pulses by transient frequency mixing in a β-barium borate crystal," Opt. Lett. **21**, 216–218 (1996).

16. R. Danelyus, G. Dikchyus, V. Kabelka, A. Piskarskas, A. Stabinis, and Ya. Yasevichyute, "Parametric excitation of light in the picosecond range," Sov. J. Quantum Electron. **7**, 1360–1368 (1977).

17. S. Fournier, R. Lopez-Martens, C. Le Blanc, E. Baubeau, and F. Salin, "Solitonlike pulse shortening in a femtosecond parametric amplifier," Opt. Lett. **23**, 627–629 (1998).

18. D. Kim and G.-Y. Xiao, "Distortion of a chirped short pulse in type II second-harmonic generation," J. Opt. Soc. Am. B **15**, 570–576 (1998).

19. P. W. Milonni, J. M. Auerbach, and D. Eimerl, "Frequency conversion modeling with spatially and temporally varying beams," Proc. SPIE **2633**, 230–241 (1997).

20. T. Nishikawa and N. Uesugi, "Effects of walk-off and group velocity difference on the optical parametric generation in KTiOPO$_4$ crystals," J. Appl. Phys. **77**, 4941–4947 (1995).

21. T. Nishikawa and N. Uesugi, "Transverse beam profiles on traveling-wave optical parametric generation in KTiOPO$_4$ crystals," J. Appl. Phys. **78**, 6361–6366 (1995).

22. G. M. Gale, M. Cavallari, and F. Hache, "Femtosecond visible optical parametric oscillator," J. Opt. Soc. Am. B **15**, 702–714 (1998).

23. B. Ruffing, A. Nebel, and R. Wallenstein, "All-solid-state cw mode-locked picosecond KTiOAsO$_4$ optical parametric oscillator," Appl. Phys. B: Photophys. Laser Chem. **67**, 537–544 (1998).

24. M. S. Bowers and S. E. Moody, "Cavity equations for a laser with an externally injected signal," J. Opt. Soc. Am. B **11**, 2266–2275 (1994).

25. A. V. Smith and M. S. Bowers, "Phase distortions in sum- and difference-frequency mixing in crystals," J. Opt. Soc. Am. B **12**, 49–57 (1995).

26. SNLO nonlinear optics software is available from A. V. Smith, Dept. 1128, Sandia National Laboratories, 87185-1423, or it may be downloaded from www site http://www.sandia.gov/imrl/XWEB1128/xxtal.htm. Methods 1 and 2 are run by the Run and Movie buttons of function PW-OPO-BB, respectively.